Journal of Microscopy, Vol. 222, Pt 1 April 2006, pp. 42–47
Received 8 July 2005; accepted 21 December 2005

Focused ion beam milling of vitreous water: prospects for an alternative to cryo-ultramicrotomy of frozen-hydrated biological samples

M. MARKO, C. HSIEH, W. MOBERLYCHAN*,
C. A. MANNELLA & J. FRANK*†
Resource for Visualization of Biological Complexity, †Howard Hughes Medical Institute, Wadsworth Center, Empire State Plaza, Albany, NY 12201, U.S.A.
**Center for Nanoscale Systems, Harvard University, 17 Oxford St., Cambridge, MA 02138, U.S.A.*

Key words. Cryo-EM, devitrification, electron tomography, FIB, frozen-hydrated specimens, vitreous ice.

Summary

The feasibility of using a focused ion beam (FIB) for the purpose of thinning vitreously frozen biological specimens for transmission electron microscopy (TEM) was explored. A concern was whether heat transfer beyond the direct ion interaction layer might devitrify the ice. To test this possibility, we milled vitreously frozen water on a standard TEM grid with a 30-keV Ga^+ beam, and cryo-transferred the grid to a TEM for examination. Following FIB milling of the vitreous ice from a thickness of approximately 1200 nm to 200–150 nm, changes characteristic of heat-induced devitrification were not observed by TEM, in either images or diffraction patterns. Although numerous technical challenges remain, it is anticipated that 'cryo-FIB thinning' of bulk frozen-hydratred material will be capable of producing specimens for TEM cryo-tomography with much greater efficiency than cryo-ultramicrotomy, and without the specimen distortions and handling difficulties of the latter.

Introduction

The promise of high-resolution three-dimensional imaging of isolated cells and organelles in the native state is being realized by cryo-electron tomography of plunge-frozen, hydrated specimens (reviewed, for example, in Frank *et al.*, 2002; Steven & Aebi, 2003; Kürner *et al.*, 2004). Extension of cryo-electron tomography to large cells and bulk, high-pressure frozen tissue requires thinning of vitreously frozen specimens to a few hundred nanometres in thickness. Cryo-ultramicrotomy of frozen-hydrated biological specimens, developed in several laboratories (e.g. Michel *et al.*, 1991; Shi *et al.*, 1996; Zhang *et al.*, 2004; Al-Amoudi *et al.*, 2005), has recently been adopted for cryo-electron tomography, and there have been reports of successful reconstruction of frozen-hydrated liver (Hsieh *et al.*, 2002, 2006), yeast (Schwartz *et al.*, 2003), isolated chloroplasts (Nicastro *et al.*, 2005) and algae (Leis *et al.*, 2005). However, cryo-ultramicrotomy is challenging, and the yield of high-resolution tomograms is low. The primary problem is lack of section flatness, which results in poor attachment of the sections to the support film, thereby making collection and alignment of tomographic tilt series problematic (Hsieh *et al.*, 2002, 2006). Frozen-hydrated sections prepared by cryo-ultramicrotomy exhibit other defects as well (e.g. Richter, 1994; Al-Amoudi *et al.*, 2005), including compression in the direction of sectioning. This compression, which is of the order of 30–50%, can cause significant distortion of cell ultrastructure. As yet, there is no reliable method either to maintain section flatness or to reduce compression in frozen-hydrated sections prepared by cryo-ultramicrotomy (Al-Amoudi *et al.*, 2003; Hsieh *et al.*, 2006).

The use of a focused ion beam (FIB) to mill frozen-hydrated specimens to a thickness suitable for electron tomography represents a possible alternative to cryo-ultramicrotomy, one that would avoid the artefacts and distortions associated with mechanical sectioning. In FIB milling, material is removed from the specimen surface by the process of sputtering. Damage to the specimen resulting from direct interaction with the ions is typically restricted to a layer that extends a few tens of nanometres into the milled surface. For example, FIB milling of crystalline silicon results in an amorphous surface layer 10–30 nm in thickness, which corresponds to the stopping range of Ga^+ ions in silicon as determined by Monte Carlo calculations (Matteson *et al.*, 2002). Based on the predicted stopping range of Ga^+ ions in 'solid water' or muscle tissue (Ziegler

Correspondence to: Michael Marko. Fax: +1 518 474 7992; e-mail: marko@wadsworth.org.
Present address of W. MoberlyChan: Materials Science and Technology Division, Lawrence Livermore National Laboratory, 7000 East Ave., Livermore, CA 94550, U.S.A.

et al., 1985), the ion interaction layer in a frozen-hydrated biological specimen would probably extend 5–20 nm into the FIB-milled surface, depending on accelerating voltage, ion current and angle of incidence. As cryo-FIB thinned frozen-hydrated specimens for TEM tomography would have a final thickness of 100–300 nm, most of the interior of these sections should be free of direct ion-beam damage.

Another concern with FIB milling of frozen-hydrated specimens is the possible transfer of thermal energy, generated in the ion interaction layer, to the interior of the specimen. This could locally raise the specimen temperature above the devitrification temperature of water, −137 °C (Dubochet *et al.*, 1988), thereby causing formation of damaging ice crystals. Because the specimen is kept at a temperature of about −150 °C on a typical FIB/SEM cold stage, even a modest temperature rise could lead to ice crystal formation.

Previously, a dual-beam FIB/SEM instrument has been used to ion-mill frozen-hydrated biological material, and to image the milled surfaces subsequently by SEM (Mulders, 2003; Gestman *et al.*, 2004). Although the milled surfaces did not appear grossly damaged in those studies, no effort was made to determine the state of the ice, either before or after FIB milling. Therefore, we undertook the experiments reported here to determine whether cryo-FIB thinning of frozen-hydrated specimens causes devitrification. Echlin (1992) notes that the presence of additional material (the protein, lipid, etc., of the biological specimen) would be expected to raise the devitrification temperature by a few degrees. Thus, we used pure water as the most sensitive specimen for this test.

Materials and methods

Water was deposited on 200-mesh copper TEM grids bearing carbon films with regularly spaced 2-μm-diameter holes (type R2/1; Quantifoil Micro Tools GmbH, Jena, Germany). The grids were plunged into liquid ethane cooled by liquid nitrogen (Dubochet *et al.*, 1988). Polystyrene latex spheres, 200 nm in diameter (Duke Scientific, Palo Alto, CA, U.S.A.), were added to the water to help to maintain the frozen layer at 100–200 nm in thickness after blotting, although local regions of thicker ice (1000 nm or greater) were often present.

TEM images were recorded with a JEM-4000FX (JEOL Ltd, Tokyo, Japan), operated at 400 kV accelerating voltage and equipped with a GIF2002 energy filter (Gatan Inc., Pleasanton, CA, USA). Zero-loss energy-filtered images were recorded with a slit width of 15 eV. The underfocus setting was 15 μm, which results in a phase-contrast transfer function with the first zero corresponding to a spacing of 5 nm. Electron diffraction patterns were recorded, unfiltered, using a FastScan F114 CCD camera (TVIPS GmbH, Gauting, Germany). Two Gatan cryo-transfer specimen holders, models 626 and CT3500TR, were used.

For the heating test, images and diffraction patterns were recorded in the TEM as the specimen was heated from −175 to −95 °C in 10 °C steps. Images and diffraction patterns were recorded from areas 2 μm in diameter, at an incident dose of 100 e^{-} nm^{-2}. Heating was carried out by adjusting the set temperature of the cryotransfer specimen holder controller. There was a 10-min waiting period after each temperature change, during which the beam was blanked. A different area of the specimen was used for each temperature step, but all of the areas were within a single 90-μm grid square, and well away from the grid bars. The heating test was performed using both 626 and CT3500TR crytotransfer holders, the latter having a stated offset of 20 °C between the indicated and actual specimen temperature. For general cryo-EM imaging, the Gatan 626 holder was used, with the specimen kept at −176 °C. The initial ice thickness used for the heating test was 150 nm.

Specimens were milled in a dual-beam DB235 FIB/SEM instrument (FEI Co., Hillsboro, OR, U.S.A.) equipped with a Gatan Alto 2500 cryo-system. The specimen was maintained at −150 °C, with the anti-contaminator at −170 °C. Specimens were milled at a nominal angle of 75° from normal (15° elevation angle from the ice surface). A relatively low ion-beam current, 10 pA, was found to be adequate, allowing milling to be performed in imaging mode, rather than in standard milling mode, so that progress of the cut could be monitored. The Ga^{+} beam had an energy of 30 keV, and a total dwell time of 38 μs per pixel was used (1024 × 1024 pixels, 0.67 μs dwell time per pixel, 57 frames, 40 s total milling time). The pixel size on the specimen was 25 nm, thus at the ion-beam current of 10 pA, the incident dose was 4 ions nm^{-2}. The expected range of Ga^{+} ions into the specimen was 15 nm, as calculated by the SRIM program (Ziegler *et al.*, 1985), using the model for 'solid water'.

Ice thickness was measured by electron energy loss, using the log-ratio method (Egerton, 1996). The absolute mean free path of 400-keV electrons in vitreous water was taken as 400 nm, based on measurements from tomograms of frozen-hydrated material (to be reported elsewhere), corrected for the ratio of the mean free paths in pure vitreous water and vitreous water with biological material (Shi *et al.*, 1996).

Results

Heating of vitreous ice in the TEM

In order to provide a direct comparison between the state of ice after FIB milling and the state of ice warmed to a specific temperature in the TEM, we recorded images and diffraction patterns from 150-nm-thick layers of plunge-frozen vitreous ice as the temperature increased from −175 to −95 °C. In these experiments, the temperature of the specimen was raised in 10 °C increments every 10 min. As shown in Fig. 1, from −165 to −145 °C, the ice retained a smooth appearance and the diffraction pattern consisted of the two diffuse rings characteristic of vitreous ice, corresponding to spacings of 0.317 and 0.214 nm. At −135 °C, spots due to Bragg diffraction from

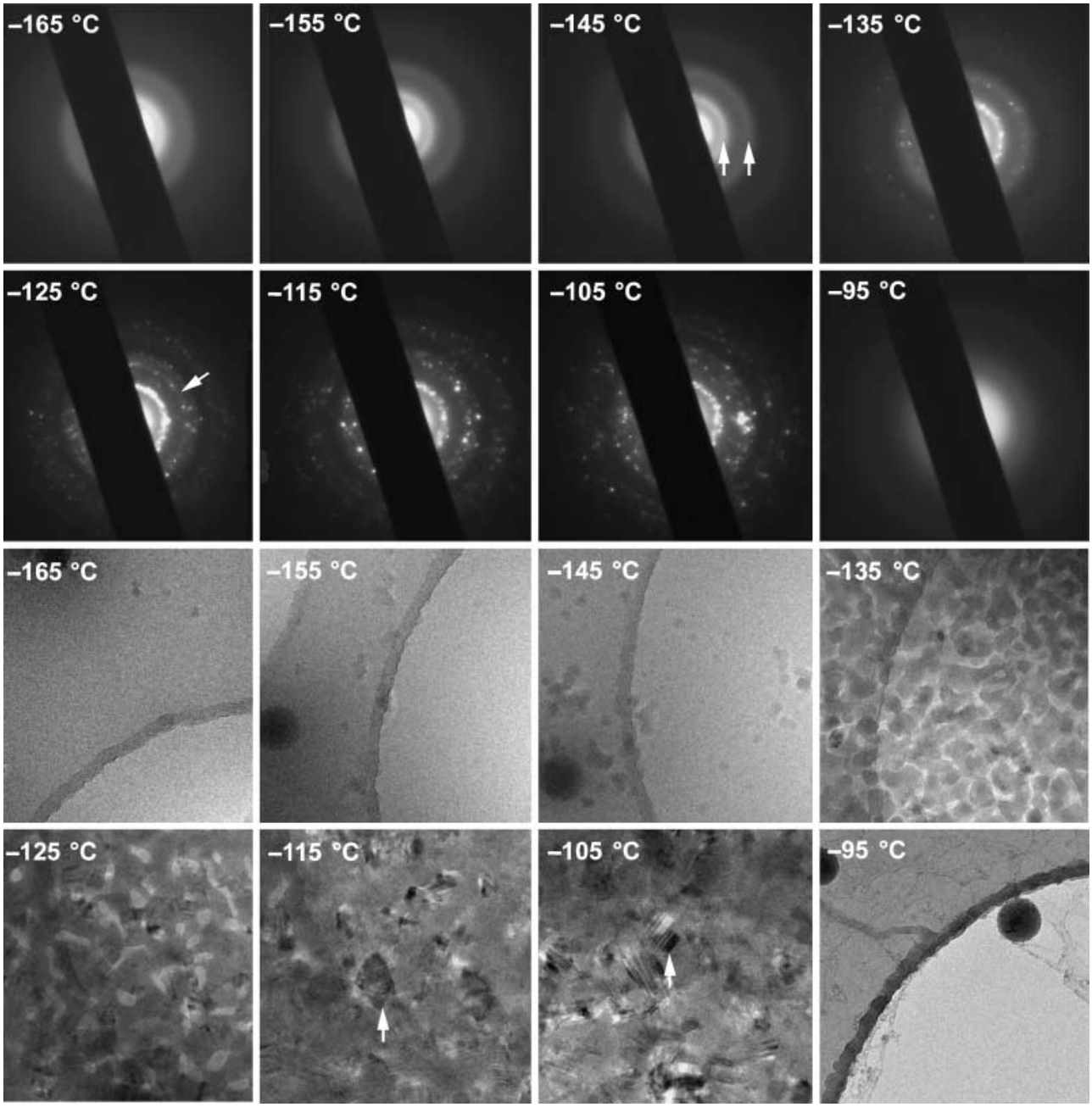

Fig. 1. Effects of temperature increase on vitrified ice. A grid of plunge-frozen water was initially maintained in the TEM at a temperature of −175 °C. Diffraction patterns (top two rows) and images (bottom two rows) were sequentially recorded, under low-dose conditions, at the temperatures indicated. A pair of diffuse rings characteristic of vitreous ice is the dominant feature in electron diffraction patterns at the lower temperatures (these two rings are indicated by arrows in the −145 °C diffraction pattern). The corresponding image, below, shows the smooth, featureless texture typical of vitreous ice. Starting at −135 °C, changes characteristic of devitrification occur in the diffraction patterns: spots caused by crystalline ice appear, and at −125 °C a faint sharp ring (arrow) characteristic of cubic ice is seen. The corresponding images show striking texture changes. At −115 and −105 °C, the ice appears completely crystalline, with prominent Bragg reflections, as indicated by the arrows. At −95 °C no ice remains. The electron-dense circles in the images at −155, −145 and −95 °C are profiles of 200-nm-diameter polystyrene spheres.

crystalline ice were superimposed on the diffuse rings from vitreous ice, and a reticular pattern was seen in the image. The reticular texture was similar to that observed when water containing a solute was frozen too slowly to form vitreous ice (Dubochet *et al.*, 1988). The observed transition from vitreous to crystalline ice was consistent with the devitrification temperature of −137 °C reported previously for pure water (Dubochet *et al.*, 1988). After offset correction, identical results were

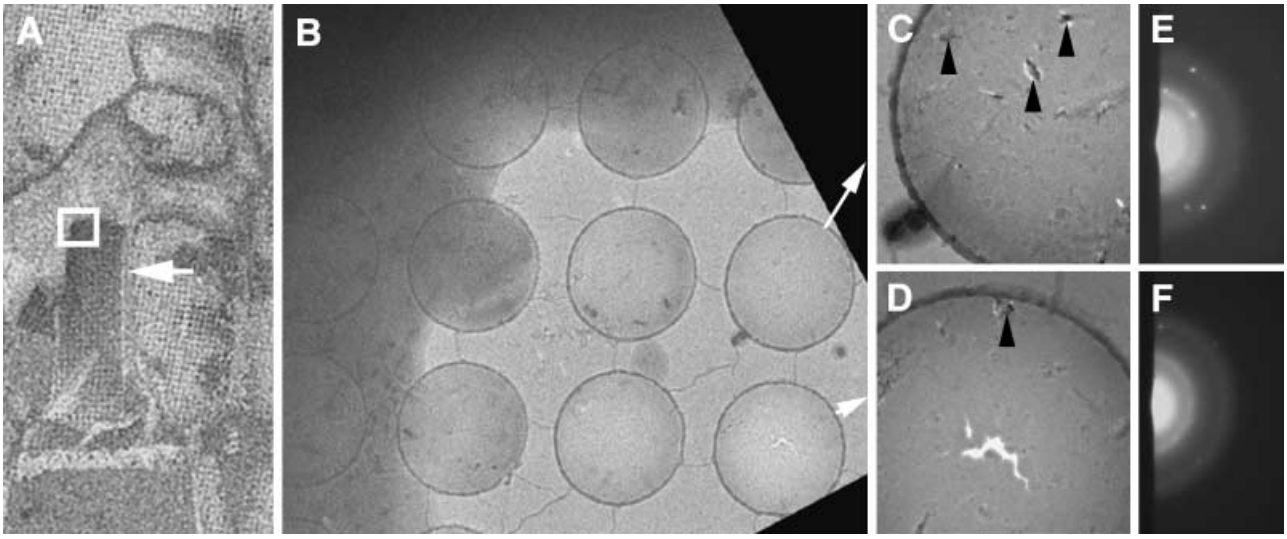

Fig. 2. FIB milling of vitreous ice. (A) SEM image of a 25-µm-wide slot (arrow) milled in a 1200-nm-thick film of vitreous ice. (B) TEM image of a corner of the slot, corresponding to the boxed region in A. (C,D) Higher magnification images of ice-covered 2-µm-diameter holes in the Quantifoil grid, as indicated by arrows in B; arrowheads indicate small frost particles of crystalline ice, presumably formed during cryo-transfer. (E,F) Diffraction patterns corresponding, respectively, to images C and D; these are dominated by the diffuse rings characteristic of vitreous ice (compare with Fig. 1).

obtained with the two different cryotransfer specimen holders, supporting the accuracy of the temperature data. As warming continued, a faint, sharp ring corresponding to the outer (0.224-nm) spacing of cubic ice was just detectable in the diffraction pattern at −125 °C, while in the image the reticular pattern was consolidating into a sheet. At −115 and −105 °C, the diffraction pattern was dominated by spots indicating hexagonal ice. The images demonstrated that the ice had consolidated into a fully crystalline sheet, and areas of dark diffraction contrast were seen in the images. At −95 °C, after 30 min of warming above the devitrification temperature, the ice had fully sublimated. These results confirmed that heating-induced devitrification of thin layers of ice can be clearly and unambiguously detected, both in the image and in the diffraction pattern.

Cryotransfer of frozen-hydrated specimens for FIB

Initial experiments with cryotransfer of the specimens into and out of the DB-235 using the Alto cryo-system were plagued by contamination with ice crystals (frost) that interfered with determination of the state of the ice in the TEM after FIB milling. The cryotransfer shuttle of the Alto consists of a small vacuum chamber with a gate valve. The walls of the chamber are at room temperature, while the cold specimen is unprotected. The transfer time is about 10 s. During this time, the specimen is subject to contamination, and perhaps to warming above the devitrification temperature. We were able to overcome this problem by constructing a special specimen holder for TEM grids. The holder has a cover that can be closed during cryotransfer, and allows mounting of the grid near the optimum angle for grazing-incidence FIB milling, without the need to pretilt the specimen stage. After transfer of the holder into the Alto preparation chamber, the cover is opened using the control rod that operates the freeze-fracture knife, and the holder is inserted into the cryo-stage. After milling, the cover is again closed before transfer out of the FIB.

FIB milling

The results of a milling experiment are shown in Fig. 2. In the SEM image of Fig. 2(A), a slot milled into a vitreously frozen water film, initially about 1200 nm thick, is visible at the arrow. A TEM image of a corner of the milled area is shown in Fig. 2(B), with a darker, unmilled region in the upper left corner. The 2-µm holes in the Quantifoil grid are clearly visible in the milled, but not in the unmilled, areas. Two of the holes in the milled region are shown at higher magnification in Fig. 2(C,D). The ice layer covering the holes is smooth, and does not show any evidence of devitrification. The reticular pattern seen in the warming experiment (Fig. 1) is absent, and the diffraction patterns (Fig. 2E,F) are dominated by two diffuse rings corresponding to spacings of 0.317 and 0.214 nm, which are characteristic of vitreous ice. A few spots are visible in the diffraction patterns; these probably originate from the small frost particles indicated by arrowheads in Fig. 2(C,D). Occasional small frost particles are inevitable with typical TEM cryotransfer practice. Using energy-loss imaging (see Materials and methods), we estimated the ice thickness in the two holes to be 200 and 150 nm in Fig. 2(C,D), respectively. We concluded that FIB milling of the layer of vitreous ice from a thickness of approximately 1200 nm to 200 nm did not

heat the remaining ice layer sufficiently to cause detectable devitrification.

The milling rate in these experiments can be estimated, but not determined precisely, because the original ice film did not have uniform thickness. In the field shown in Fig. 2(A), a wedge-shaped volume of ice, approximately 200 μm^3, was removed within 40 s, at the relatively low ion current of 10 pA, giving an approximate milling rate of 5 $\mu m^3 s^{-1}$. In other experiments, when varying the milling parameters over a wide range, we found that for a given protocol the milling rate for vitreous water was always at least 100 times higher than that for silicon.

The conditions used in these experiments, in regard to ion-beam energy, angle of incidence and dose rate, did not minimize the depth of the Ga^+ ion interaction layer. In practice, by performing final milling at 5 keV instead of 30 keV, and by using an incidence angle more nearly parallel to the specimen surface, the damage layer could probably be kept to around 5 nm.

Discussion

A primary goal of cryo-electron tomography is to understand the three-dimensional macromolecular organization of the cell in its native state. For routine application of cryo-electron tomography to large cells and mammalian tissue, means are needed to produce suitably thin specimens from bulk frozen material. Frozen-hydrated sections produced by cryo-ultramicrotomy have physical defects (lack of flatness, compression) that affect structural fidelity and complicate collection and alignment of tomographic tilt series. These limitations are of sufficient concern to warrant exploration of alternative approaches to prepare thin specimens from bulk vitreously frozen material, such as milling with a focused ion beam.

The results presented in this report establish a critically important fact: FIB milling of vitreous ice does not induce heating sufficient to cause devitrification. This is a necessary condition for cryo-FIB thinning to be considered for development as an alternative to cryo-ultramicrotomy for preparing thin, frozen-hydrated biological specimens for cryo-TEM. Several key engineering challenges will need to be addressed in order to develop this methodology further. Of foremost importance are the design of convenient stages and transfer devices, and the formulation of milling strategies that yield geometries that maximize tilt range and stability during tomographic data recording, while minimizing milling time.

We estimate that, by the use of coarse rapid milling followed by finer 'clean-up' milling, it should be possible to mill a specimen area 200 nm thick and 50–100 μm square from a 200-μm-thick block of frozen tissue in a matter of a few hours. Mechanical pretrimming, which does not cause distortion of the bulk specimen (Walther & Müller, 1999) could speed up this process. As modern FIB instruments are programmable, allowing precise and reproducible specimen milling, several different regions of a specimen block could conveniently be sampled in a single specimen for TEM.

In cryo-ultramicrotomy, sections suffer from in-plane compression and lack of flatness that currently can be neither avoided nor corrected. These are the main factors that prevent the routine application of cryo-TEM tomography to native biological tissue (Hsieh *et al.*, 2002, 2006). Efficient production of frozen-hydrated samples suitable for high-resolution cryo-TEM tomography, by means of cryo-FIB thinning, would represent a major advance in three-dimensional biological electron microscopy.

Acknowledgements

We thank George Matuszek and Steven Meyer of the Wadsworth Center for constructing the cryo-transfer specimen holder, and Dr Lucille Giannuzzi of FEI for advice and encouragement. This work was supported by NIH/NCRR Biomedical Research Technology Program Grant RR01219 (P.I. J. Frank), which funds the Wadsworth Center's Resource for Visualization of Biological Complexity.

References

Al-Amoudi, A., Dubochet, J., Gnägi, H., Lüthi, W. & Studer, D. (2003) An oscillating cryo-knife reduces cutting-induced deformation of vitreous ultrathin sections. *J. Microsc.* **212**, 26–33.

Al-Amoudi, A., Studer, D. & Dubochet, J. (2005) Cutting artifacts and cutting process in vitreous sections for cryo-electron microscopy. *J. Struct. Biol.* **150**, 109–121.

Dubochet, J., Adrian, M., Chang, J.J., Homo, J.-C., Lepault, J., McDowall, A.W. & Schultz, P. (1988) Cryo-electron microscopy of vitrified specimens. *Quart. Rev. Biophys.* **21**, 129–228.

Echlin, P. (1992) *Low-Temperature Microscopy and Microanalysis*. Plenum Press, New York.

Egerton, R.F. (1996) *Electron Energy-Loss Spectroscopy in the Electron Microscope*, 2nd edn. Plenum Press, New York.

Frank, J., Wagenknecht, T., McEwen, B.F., Marko, M., Hsieh, C.-E. & Mannella, C.A. (2002) Three-dimensional imaging of biological complexity. *J. Struct. Biol.* **138**, 85–91.

Gestman, I., Hayles, M., Shi, D., Kumar, G., Giannuzzi, L., Lich, B. & Subramaniam, S. (2004) Site-specific 3D imaging of cells and tissues using dualbeam technology. *Miscrosc. Microanal.* **10** (Suppl. 2), 1124CD.

Hsieh, C.-E., Leith, A., Mannella, C.A., Frank, J. & Marko, M. (2006) Towards high-resolution three-dimensional imaging of native mammalian tissue: electron tomography of frozen-hydrated rat liver sections. *J. Struct. Biol.* **153**, 1–13.

Hsieh, C.-E., Marko, M., Frank, J. & Mannella, C.A. (2002) Electron tomographic analysis of frozen-hydrated tissue sections. *J. Struct. Biol.* **138**, 63–73.

Kürner, J., Medalia, O., Linaroudis, A.A. & Baumeister, W. (2004) New insights into the structural organization of eukaryotic and prokaryotic cytoskeletons using cryo-electron tomography. *Exp. Cell Res.* **301**, 38–42.

Leis, A., Andrees, L., Gruska, M., Al-Amoudi, A., Sartori, A., Dubochet, J. & Baumeister, W. (2005) Cryo-electron tomography and fluorescence

microscopy of unicellular algae in vitreous cryosections. *Microsc. Microanal.* **11** (Suppl. 2), 330CD.

Matteson, T.L., Schwartz, S.W., Houge, E.C., Kempshall, B.W. & Giannuzzi, L.A. (2002) Electron backscattering diffraction investigation of focused ion beam surfaces. *J. Electron. Mat.* **31**, 33–39.

Michel, M., Hillman, T. & Müller, M. (1991) Cryosectioning of plant material frozen at high pressure. *J. Microsc.* **163**, 3–18.

Mulders, H. (2003) The use of a SEM/FIB dual beam applied to biological samples. *G.I.T. Imaging Microsc.* **2**, 8–10.

Nicastro, D., Austin, J., Pierson, J., Gaudette, R., Schwartz, C., Ladinsky, M., Staehelin, L.A. & McIntosh, J.R. (2005) Visualizing the macromolecular organization of chloroplast membranes using cryo-electron tomography. *Microsc. Microanal.* **11** (Suppl. 2), 150–151.

Richter, K. (1994) Cutting artefacts on ultrathin cryosections of biological bulk specimens. *Micron*, **25**, 297–308.

Schwartz, C., Nicastro, D., Ladinsky, M.S., Mastronarde, D., O'Toole, E. & McIntosh, J.R. (2003) Cryo-electron tomography of frozen-hydrated sections of eukaryotic cells. *Microsc. Microanal.* **9** (Suppl. 2), 1166–1167.

Shi, S., Sun, S.Q., Andrews, B. & Leapman, R.D. (1996) Thickness measurement of hydrated and dehydrated cryosections by EELS. *Microsc. Res. Techn.* **33**, 241–250.

Steven, A.C. & Aebi, U. (2003) The next ice age: cryo-electron tomography of intact cells. *Trends Cell Biol.* **13**, 107–110.

Walther, P. & Müller, M. (1999) Biological ultrastructure as revealed by high resolution cryo-SEM of block faces after cryo-sectioning. *J. Microsc.* **196**, 279–287.

Zhang, P., Bos, E., Heyman, J., Gnägi, H., Kessel, M., Petere, P.J. & Subramaniam, S. (2004) Direct visualization of receptor arrays in frozen-hydrated sections and plunge-frozen specimens of *E. coli* engineered to overproduce the chemotaxis receptor Tsr. *J. Microsc.* **216**, 76–83.

Ziegler, J.F., Biersack, J.P. & Littmark, U. (1985) *The Stopping and Range of Ions in Solids*. Pergamon Press, New York.